Analysis and Modeling of Interharmonics From Grid-Connected Photovoltaic Systems

Ariya Sangwongwanich, *Student Member, IEEE*, Yongheng Yang, *Senior Member, IEEE*, Dezso Sera, *Senior Member, IEEE*, Hamid Soltani, *Member, IEEE*, and Frede Blaabjerg, *Fellow, IEEE*

***Abstract*—The industry of solar photovoltaic (PV) energy and its application is still booming to enhance the sustainability of the society. When PV systems are connected to the grid, challenging issues should be addressed. One of the challenges is related to interharmonics in PV systems, especially with a large-scale adoption of PV systems. However, the origins of interharmonics remain unclear, although the impact of interhamonics has been reported in the literature. Thus, this paper explores the generation mechanisms of interharmonics in PV systems and the characteristics. The exploration reveals that the perturbation from the maximum power point tracking (MPPT) algorithm is one of the origins of interharmonics appearing in the grid current. Accordingly, the MPPT controller parameters such as the perturbation step size and the sampling rate have an inevitable impact on the interharmonic characteristics. Furthermore, an approach to characterize the interharmonics in the grid current is proposed. With the proposed model, interharmonics can be predicted according to the designed controller parameters in terms of frequencies and amplitudes. Experimental tests are performed on a single-phase grid-connected PV system. The results are in a close agreement with the analysis and, thus, validate the effectiveness of the proposed model.**

***Index Terms*—Interharmonics, inverters, maximum power point tracking (MPPT), modeling, photovoltaic (PV) systems, power quality.**

I. Introduction

In RECENT years, more and more photovoltaic (PV) systems have been installed and connected to the grid due to the increasing demand of greener and more sustainable energy systems. However, at the same time, massive connections of PV systems to the grid bring several challenges, e.g., power quality and grid stability issues [1]–[6]. It has been reported that the grid-connected PV systems might be one source of harmonics including interharmonics delivered to the grid, which leads to a poor power quality [7]–[12]. In the latest research, many attempts have been made to identify the impact of harmonics from grid-connected PV inverters. In general, harmonics are generated by PV inverters due to the nonideal switching behaviors of the power devices (e.g., the deadtime effect) and also the interaction among different controllers (e.g., the dc-link voltage and the current controllers) [13]–[15]. Solutions to mitigate harmonics can also be found in the literature [11]–[15]. On the other hand, the interharmonic issues in PV systems are rarely discussed. Nevertheless, it has been revealed in a few recent publications that a large-scale adoption of grid-connected PV inverters may contribute to interharmonics in the grid currents, causing overloading and flickering [16]–[22]. In the worst scenario, interharmonics may trigger the protection circuit, and thus, the PV systems are unintentionally disconnected from the grid [18]. Consequences of such events include considerable energy losses and challenges in the system stability in the case of large-scale PV systems. As the penetration level of PV systems is still increasing, the impact of interharmonics cannot be overlooked. Therefore, the interharmonic issues of PV inverters should be explored and analyzed in order to develop proper mitigation approaches.

By definition, interharmonics are frequency components with noninteger times of the fundamental frequency (e.g., 50 Hz in Europe). In other words, interharmonics can be discrete frequency components (i.e., a single frequency component) or distortion signals with a wideband spectrum in some in-between integer harmonics [23]. In this regard, the detection of interharmonics is challenging in practice [24]. Concerning the generation of interharmonics, there are several possibilities in power electronic systems [23]: two asynchronous conversion systems (e.g., motor drives) [25]–[27], time-varying loads (e.g., arc furnaces) [28], and mechanical vibrations (e.g., in wind turbines) [29]. Among those, PV systems are usually not considered as a source of interharmonics, since it is typically viewed as a single dc–ac conversion system. However, as the maximum power point tracking (MPPT) control is mandatory in PV systems and it imposes variations in the dc power during the maximum power point (MPP) searching, interharmonics may also be generated from PV systems [19]–[21]. This has been observed experimentally with some commercial PV inverters [19]–[22], where a considerable amount of interharmonics from PV inverters have been measured during the steady-state MPPT operation. Specif-

Manuscript received July 20, 2017; revised October 9, 2017; accepted November 20, 2017. Date of publication January 1, 2018; date of current version July 15, 2018. This work was supported in part by the European Commission within the European Union's Seventh Framework Program (FP7/2007-2013) through the SOLAR-ERA.NET Transnational Project (PV2.3-PV2GRID) and ERC Grant 321149-Harmony, and in part by the Research Promotion Foundation under Project KOINA/SOLAR-ERA.NET/0114/02. This study has also been supported by VILLUM FONDEN under the VILLUM Investigators Grant — Reliable Power Electronic based Power System (REPEPS). Recommended for publication by Associate Editor A. K. Gupta. *(Corresponding author: Yongheng Yang.)*

A. Sangwongwanich, Y. Yang, D. Sera, and F. Blaabjerg are with the Department of Energy Technology, Aalborg University, Aalborg DK-9220, Denmark (e-mail: ars@et.aau.dk; yoy@et.aau.dk; des@et.aau.dk; fbl@et.aau.dk).

H. Soltani is with the R&D Converter Control Engineer, Vestas Wind Systems A/S, Aarhus N 8200, Denmark (e-mail: hasol@vestas.com).

Color versions of one or more of the figures in this paper are available online at http://ieeexplore.ieee.org.

Digital Object Identifier 10.1109/TPEL.2017.2778025

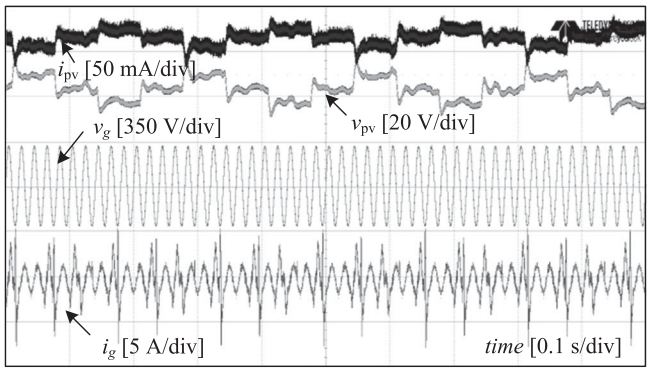

Fig. 1. Experimental results from a commercial 15-kW PV inverter operating at 2% of the rated power (i.e., MPPT operation), where v_{pv} is the PV voltage, i_{pv} is the PV current, v_g is the grid voltage, and i_g is the grid current.

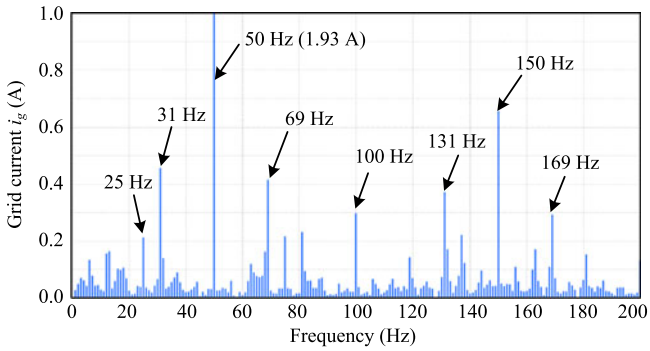

Fig. 2. Frequency spectrum of the grid current from the measurements shown in Fig. 1 with a frequency resolution of 1 Hz.

ically, it is suggested in [19]–[21] that the interharmonic frequency spectrum is correlated with the MPPT frequency.

Similar characteristics have also been observed in a commercial PV inverter tested at Aalborg University. The test results are shown in Fig. 1 and the frequency spectrum presented in Fig. 2 demonstrates that there are interharmonics in the injected grid current. This can be clearly seen when the PV inverter operates at low-power conditions. Furthermore, as shown in Fig. 2, the interharmonics appear as a series of low-frequency components and to some extent, in agreement with the observations seen in a previous study [20]. Nevertheless, the designed controller parameters of the commercial PV inverter under test are not available. Thus, mapping the interharmonic frequency to the MPPT or other controller frequencies from the experimental data is a difficult task. That is, the mechanism of the interharmonic emission is not yet fully understood, and the above analysis is done still from observations of measurements. Although a brief discussion on the interharmonic emission mechanisms through simulations has been presented in [30], an in-depth analysis of the mechanisms is still absent and has not been validated experimentally either. Moreover, the influence of controller parameters (e.g., the MPPT controller parameters) on the interharmonic characteristics has not been explored. In all, it calls for a more detailed modeling and a thorough analysis of the interharmonics in grid-connected PV systems.

Accordingly, this paper explores the mechanisms of interharmonic emissions from grid-connected PV systems in Section II.

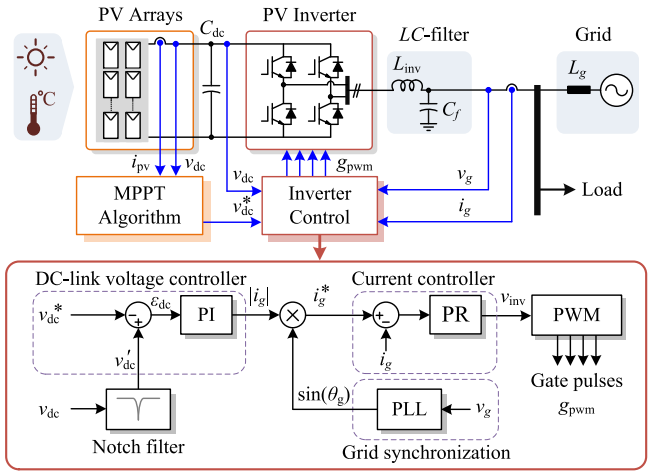

Fig. 3. System configuration and control structure of single-phase grid-connected PV systems in the MPPT operation mode (PI—proportional integral; PR—proportional resonant; PWM—pulse width modulation; PLL—phase-locked loop).

TABLE I
PARAMETERS OF THE SINGLE-PHASE GRID-CONNECTED PV SYSTEM

PV rated power	3 kW
DC-link capacitor	$C_{dc} = 1100\ \mu$F
LC-filter	$L_{inv} = 4.8$ mH, $C_f = 4.3\ \mu$F
Leakage inductance of the transformer	$L_g = 2$ mH
Switching frequency	$f_{inv} = 8$ kHz
Controller sampling frequency	$f_s = 20$ kHz
DC-link voltage	$v_{dc}^* = 450$ V
Grid nominal voltage (RMS)	$V_g = 230$ V
Grid nominal frequency	$f_g = 50$ Hz

It has been observed on a 3-kW single-phase PV system in Section II that the perturbation of the MPPT operation is one of the main root causes of interharmonics. The influence of the controller parameters, such as the perturbation step size and the MPPT algorithm sampling rate, on the interharmonics has also been investigated in Section III. Furthermore, an analytical model is proposed to identify interharmonics according to the predesigned controller parameters. The analysis results are shown in Section IV, which agree well with the experimental tests in Section III. This validates the feasibility of the proposed model for interharmonic analysis and identification. Finally, concluding remarks are given in Section V.

II. CONTROL AND OPERATION OF SINGLE-PHASE GRID-CONNECTED PV INVERTERS

A. System Configuration and Control Structure

In order to investigate the interharmonics from grid-connected PV systems, experimental tests have been conducted on a single-phase single-stage grid-connected PV system. The system configuration is shown in Fig. 3. The experimental setup shown in Fig. 4 is employed and the system parameters are given in Table I. A PV simulator (Chroma 62000H-S) is employed to emulate the PV array characteristic during the test [31]. With the simulator, it is possible to program the PV array characteristic such as the maximum available power and the voltage at the MPP in order to make the test condition repeatable to

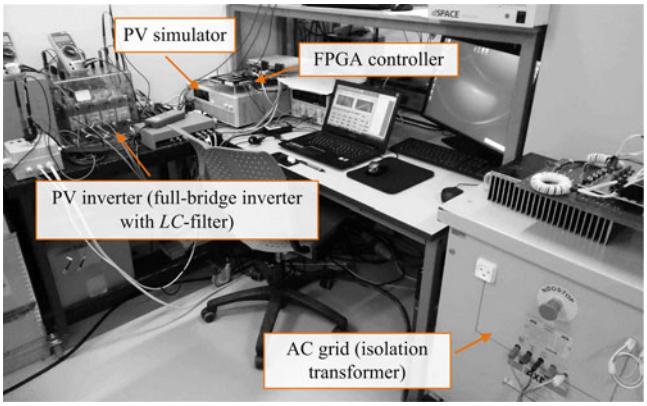

Fig. 4. Experimental setup of a single-phase single-stage grid-connected PV system to explore interharmonics.

compare different cases (e.g., different control parameters). The PV inverter is connected to the grid through an LC filter and an isolation transformer in order to provide a galvanic isolation between the PV array and the grid.

With this single-stage configuration, the PV inverter (e.g., the full-bridge inverter) plays a major role in controlling the power delivery from the PV arrays to the ac grid [32]. In order to ensure the maximum power extraction from the PV arrays, an MPPT algorithm (e.g., perturb and observe—P&O) is employed to determine the reference dc-link voltage $v_{\rm dc}^*$ (i.e., the PV voltage) during operation. Then, the dc-link voltage controller, e.g., a proportional integral (PI) controller, regulates the dc-link voltage $v_{\rm dc}$ accordingly through the control of the amplitude of the grid current $|i_g|$. The reference grid current i_g^* is generated considering the phase of the grid voltage $\sin(\theta_g)$, which is obtained from a phase-locked loop (PLL). For single-phase systems, the dc-link voltage $v_{\rm dc}$ contains double-line frequency components (e.g., 100 Hz) [33]. Thus, a notch filter is used to improve the dc-link voltage control performance [33], [34].

The control performance of the PV system is demonstrated by introducing a step change in the reference dc-link voltage $v_{\rm dc}^*$ at $t = 2$ s. It can be seen from the experimental results in Fig. 5 that the dc-link voltage $v_{\rm dc}$ can quickly follow a change of the set-point $v_{\rm dc}^*$. The injected grid current also react to the change, as the dc-link voltage error [see Fig. 5(c)] is used to generate the amplitude of the grid current reference. The frequency spectrum of the grid current during the steady-state operation is shown in Fig. 6, where a constant dc-link voltage reference is applied (i.e., the MPPT control is disabled). It can be seen in Fig. 6 that the grid current i_g contains only the fundamental-frequency component (i.e., 50 Hz). In other words, the interharmonics in the grid current are negligible under this operating condition. The experiment implies that the interharmonics are potentially related to the dc-link control, more specifically, the dc-link voltage reference.

B. MPPT Operation

According to [19]–[21] and [30], the MPPT operation is considered as a source of interharmonics in PV systems. Therefore, the performance of PV systems under the MPPT operation is

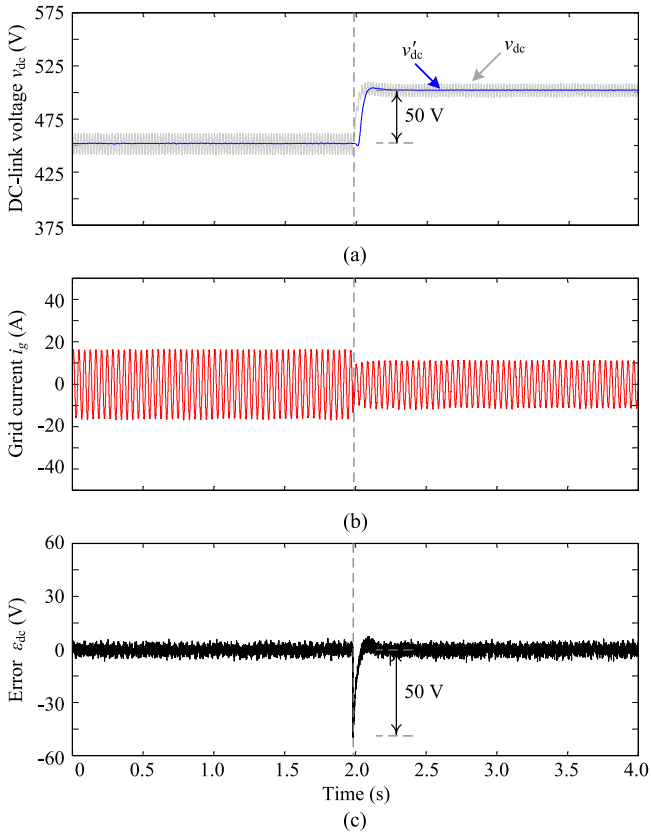

Fig. 5. Experimental results of the PV inverter during a step change in the reference dc-link voltage from $v_{\rm dc}^* = 450$ V to $v_{\rm dc}^* = 500$ V (i.e., the PV power is reduced) at $t = 2$ s: (a) dc-link voltage ($v_{\rm dc}$ is the measured dc-link voltage, $v'_{\rm dc}$ is the dc component of $v_{\rm dc}$), (b) grid current i_g, and (c) error in the dc-link voltage $\varepsilon_{\rm dc}$.

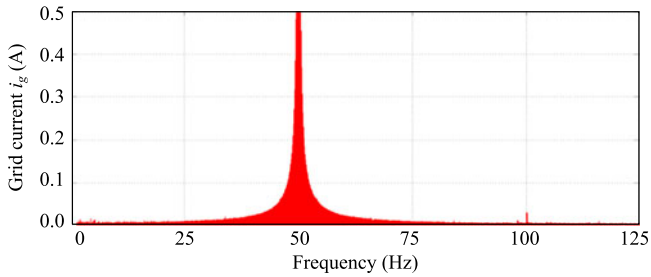

Fig. 6. Frequency spectrum of the grid current i_g during the constant dc-link voltage operation at 100% of the rated power (i.e., 3 kW) with the frequency resolution of 0.125 Hz.

investigated in this section. Here, the P&O MPPT algorithm is employed due to its simplicity. In fact, the P&O MPPT algorithm is one of the most widely used MPPT algorithms in industry [35], and its performance has also been observed previously from the test on the commercial PV inverter in Fig. 1.

One important characteristic of the P&O MPPT algorithm (and also other hill-climbing-type MPPT algorithms) is the power oscillation during the steady-state operation (e.g., even under a constant solar irradiance condition) [35]. This can be clearly seen from the experimental results in Figs. 7 and 8, where the PV system operates in the steady-state condition with a constant solar irradiance and ambient temperature condition

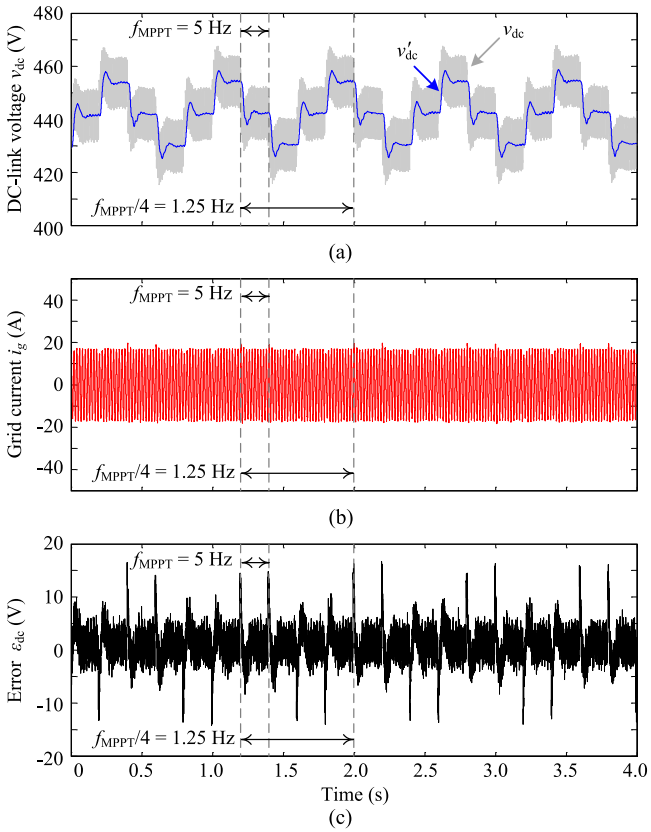

Fig. 7. Experimental results of the PV inverter operated at 100% of the rated power (i.e., 3 kW) in steady-state MPPT operation (MPPT sampling rate f_{MPPT} = 5 Hz, the perturbation step size v_{step} = 12 V): (a) dc-link voltage (v_{dc} is the measured dc-link voltage, v'_{dc} is the dc component of v_{dc}), (b) grid current i_g, and (c) error in the dc-link voltage ε_{dc}.

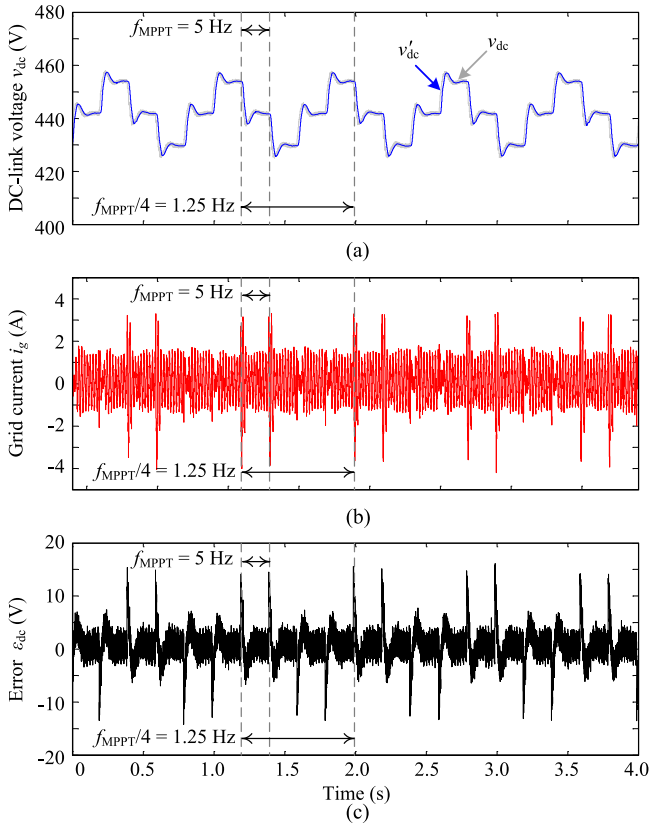

Fig. 8. Experimental results of the PV inverter operated at 10% of the rated power (i.e., 300 W) in a steady-state MPPT operation (MPPT sampling rate f_{MPPT} = 5 Hz, the perturbation step size v_{step} = 12 V): (a) dc-link voltage (v_{dc} is the measured dc-link voltage, v'_{dc} is the dc component of v_{dc}), (b) grid current i_g, and (c) error in the dc-link voltage ε_{dc}.

at 100% and 10% of the rated power, respectively. Notably, the controller parameters (e.g., PI controller parameters, MPPT perturbation step size v_{step}, and MPPT algorithm sampling rate f_{MPPT}) are identical for both operating conditions. In those cases, the MPPT operation is stable and the dc-link voltage v_{dc} (i.e., the PV voltage) oscillates around three optimum operating points with the MPPT algorithm sampling frequency f_{MPPT} of 5 Hz. This is considered as the optimal MPPT operation, as it is discussed in [36], and similar behaviors have been observed in the commercial PV inverter, as shown in Fig. 1. However, it can be noticed that the injected grid current i_g is distorted due to the perturbation, which can be clearly seen at the low-power operation in Fig. 8(b). In that case, the injected grid current i_g presents a large overshoot during the perturbation of the dc-link voltage v_{dc}. Since this perturbation will be repeated periodically (during the steady-state operation), interharmonics are generated in the grid current, which will be analyzed in detail in the following.

C. Interharmonic Characteristics

The interharmonics characteristic can be characterized considering the frequency components in the grid current i_g. Fig. 9 shows the frequency spectrum of the grid current from the PV system operated at different power levels (i.e., 100% and 10% of the rated power). The measurements have been carried out

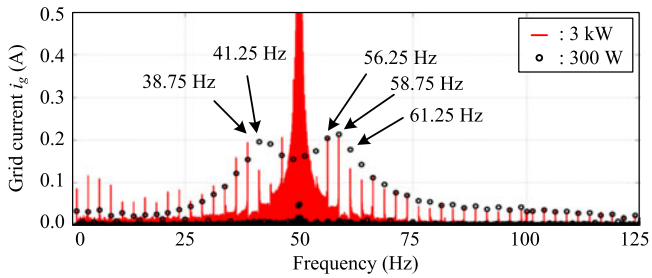

Fig. 9. Frequency spectrum of the grid current i_g during the steady-state MPPT operation at 100% of the rated power, i.e., 3 kW (red line) and 10% of the rated power, i.e., 300 W (black dot) with the frequency resolution of 0.125 Hz.

for 8 s during the test (only half of the time-domain waveforms are shown in Figs. 7 and 8). Therefore, the frequency spectrum can be analyzed with a frequency resolution of 1/8 = 0.125 Hz. It can be seen from the results in Fig. 9 that the interharmonics in the grid current appear as a series of frequency components with a constant distance between each consecutive component. The envelope of the frequency component is almost symmetrical around the fundamental-frequency component of the grid current. This resembles to the test results from the commercial PV inverter in Fig. 2 and also in the literature [20]. In this case, the distance between each consecutive interharmonic frequency is 2.5 Hz (e.g., 56.25 Hz, 58.75 Hz, 61.25 Hz, ...). This is ap-

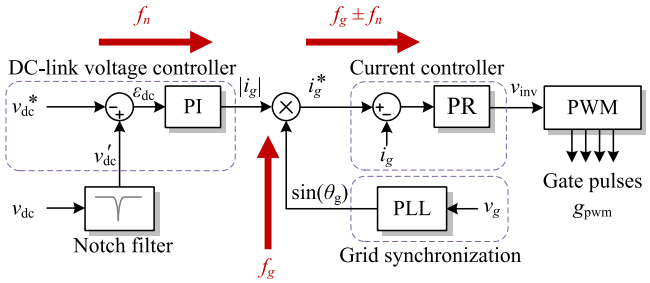

Fig. 10. Frequency mapping of different controllers in the grid-connected PV inverter, where f_n is the frequency of the error in the dc-link voltage, and f_g is the fundamental grid frequency.

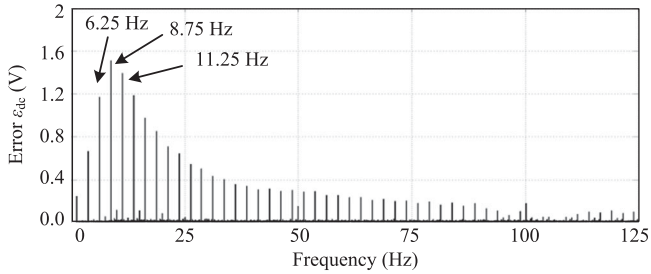

Fig. 11. Frequency spectrum of the error in the dc-link voltage ε_{dc} during the steady-state MPPT operation at 10% of the rated power (i.e., 300 W) with a frequency resolution of 0.125 Hz.

plied for the operation at 100% and 10% of the rated power. In both cases, the interharmonics appear at the same frequencies. Moreover, the amplitudes of the interharmonics are also similar (in absolute values), although the amplitude of the fundamental-frequency component at 100% of the rated power is around 10 times higher than that at 10% of the rated power.

D. Interharmonic Emission Mechanism

It is necessary to understand the root causes of interharmonics in order to map the interharmonic characteristics with the control parameters. From the results in Fig. 8, it can be seen that the interharmonics in the grid current are induced by the MPPT perturbation, where the reference dc-link voltage v_{dc}^* experiences step changes with an amplitude corresponding to the MPPT perturbation step size v_{step}. This will result in an error ε_{dc} at the input of the dc-link voltage controller, as shown in Fig. 8(c). Due to the periodic MPPT perturbation, the error in the dc-link voltage ε_{dc} is also a periodic waveform, which contains a set of frequency components f_n. Since the dc-link voltage controller is the outer control loop (see Fig. 3), the frequency components of the dc-link voltage error ε_{dc} can propagate to the grid current amplitude reference $|i_g|$. Then, the multiplication between the grid current amplitude reference $|i_g|$ and the phase of the grid voltage $\sin(\theta_g)$ will induce an amplitude modulation between the two signals. As a consequence, the reference grid current i_g^* will contain the frequency components of $f_g \pm f_n$, where f_g is the fundamental grid frequency. Assuming an ideal current controller, the injected grid current i_g will follow its reference i_g^*, inducing the interharmonic components with the frequencies being $f_g \pm f_n$ in the grid current. Fig. 10 summarizes the frequency mapping of each part in the control structure. Notably, the response of the MPPT perturbation is almost independent on the operating power of the PV system, as it can be seen in Figs. 7(c) and 8(c). Consequently, the interharmonic characteristics in the grid current under both operating conditions (i.e., 100% and 10% of the rated power) are similar in terms of frequency and amplitude.

To verify the above analysis, the frequency spectrum of the error in the dc-link voltage is shown in Fig. 11. It can be observed in Fig. 11 that the frequency of the interharmonic components is $f_n = (2n-1)f_{MPPT}/4$, where f_{MPPT} is the MPPT algorithm sampling frequency and n is an integer number (e.g., $f_n =$ 1.25 Hz, 3.75 Hz, 6.25 Hz,... for $f_{MPPT} = 5$ Hz). The dominant frequency components with high amplitudes are around 6.25 Hz, 8.75 Hz, and 11.25 Hz. If the grid voltage only contains the fundamental-frequency component (e.g., $f_g = 50$ Hz), which is the case in this experiment, the dominant frequencies after the amplitude modulation should be 38.75 Hz, 41.25 Hz, and 43.75 Hz (i.e., $f_g - f_n$) and 56.25 Hz, 58.75 Hz, and 61.25 Hz (i.e., $f_g + f_n$). This is in a close agreement with the frequency spectrum of the grid current shown in Fig. 9. Thus, the above analysis in terms of frequency mapping is valid. In order to further analyze the amplitude of each interharmonic component, a control system model is required for determining the system response due to the MPPT perturbation. This will be explained in Section IV.

III. Controller Parameter Impact on Interharmonics

In the above discussion, the interharmonics have been observed in the grid current during the MPPT operation. Although the experimental results suggest that the interharmonic characteristics of the grid current are almost not affected by the operating power of the PV system, the controller parameters may have certain impacts. More specifically, the parameters of the MPPT algorithm may change the interharmonic characteristics according to the frequency mapping in Fig. 10. The perturbation step size v_{step} and the sampling rate f_{MPPT} are two typical parameters of the MPPT algorithms, whose influence on the interharmonics will be discussed in the following.

A. Impact of the MPPT Perturbation Step Size

The perturbation step size v_{step} strongly affects the tracking performance of the MPPT algorithms. A large step size can improve the tracking speed due to the reduced number of iterations (e.g., during the solar irradiance change) and also increase the noise immunity (e.g., due to ripples in the dc-link voltage and measurement noise) [36]. However, it will result in large power oscillations during steady-state operation, increasing the power losses and thus lowering the overall efficiency.

This phenomenon is demonstrated in Fig. 12, where three different perturbation step sizes of $v_{step} = 6$ V, 12 V, and 18 V are employed in the P&O MPPT algorithm. Observations in Fig. 12 indicate that the step size clearly affects the interharmonics. Notably, the operating power of the PV system is kept at 10 % of the rated power (i.e., 300 W) for all cases, where the impact of the perturbation step size can be clearly seen in

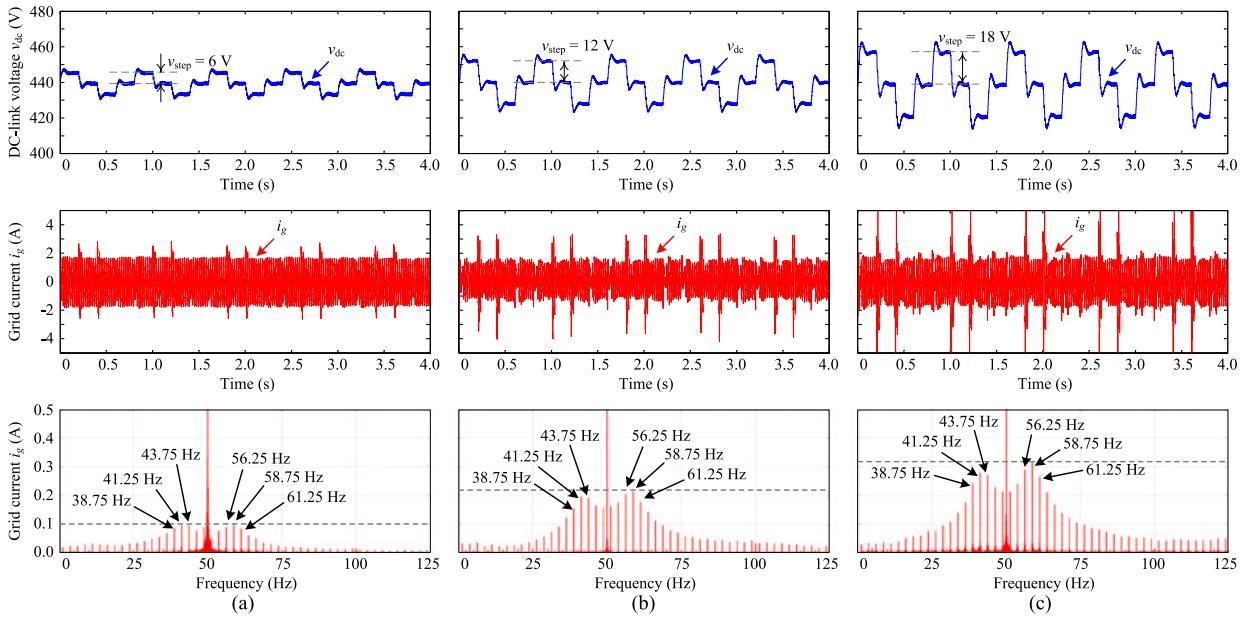

Fig. 12. Experimental results of the PV system operating at 10% of the rated power (i.e., 300 W) with the MPPT perturbation step size of (a) $v_{\text{step}} = 6$ V, (b) $v_{\text{step}} = 12$ V, and (c) $v_{\text{step}} = 18$ V, where v_{dc} is the dc-link voltage (PV voltage), and i_g is the grid current.

the time-domain waveforms of the grid current i_g (the amplitude of the interharmonic component becomes comparable with the fundamental frequency component). The other control parameters (e.g., parameters for the PI and current controllers) are identical. It can be concluded from the above tests that large step sizes will result in higher overshoots in the grid current during the perturbation. The corresponding frequency spectrum of the grid current is analyzed and also shown in the same figure. It further confirms that the perturbation step size has a strong influence on the amplitude of the interharmonic components. However, it is worth mentioning that the frequencies of the interharmonics are the same regardless of the perturbation step size amplitude, implying that the a frequency is not dependent on the perturbation step size.

B. Impact of the MPPT Sampling Rate

Another important parameter of MPPT algorithms is the sampling rate f_{MPPT}. Increasing the MPPT sampling rate can improve the tracking performance in the case of fast solar irradiance changes. However, the maximum sampling rate of an MPPT algorithm is limited by the dynamic of the dc-link voltage controller, as the dc-link voltage (PV voltage) should reach the steady-state operation before applying the next perturbation. Typically, the MPPT sampling rate is about 1–20 Hz [37]–[39].

In this paper, three MPPT sampling rates (i.e., $f_{\text{MPPT}} = 2$, 5, and 10 Hz) are chosen. The grid currents with different MPPT sampling rates are shown in Fig. 13. Clearly, the perturbation in the grid current occurs more frequently as the MPPT sampling rate increases. On the other hand, the overshoot in the grid current is almost the same with the three MPPT sampling rates. Furthermore, when seeing from the frequency spectrum of the grid current in Fig. 13, the frequency distance between the consecutive interharmonic component increases along with the MPPT sampling rate. The same observations go for the amplitude of the interharmonic components, although the perturbation step size v_{step} is the same for all cases. This brings more insights into the design of MPPT algorithms—increasing the MPPT sampling rate may challenge the power quality of the injected grid current in terms of interharmonics.

IV. Modeling of Interharmonics

As discussed in Section III, the controller parameters (e.g., the perturbation step size v_{step} and the MPPT sampling rate f_{MPPT}) strongly affect the interharmonics in the grid current. In order to map the interharmonic characteristic with the designed controller parameters, modeling of interharmonics is presented in this section. The flow diagram of the interharmonic modeling is illustrated in Fig. 14, where three modeling parts are involved: 1) periodic MPPT oscillation; 2) response of the dc-link voltage perturbation; and 3) amplitude modulation.

A. Periodic MPPT Oscillation

Since the main cause of interharmonics in the grid current is the MPPT perturbation, the representation of the dc-link voltage during the MPPT perturbation is required as an input to the analysis. In that case, the Fourier analysis should be applied to the variation in the reference dc-link voltage during the MPPT operation. Due to the power oscillation characteristic of the P&O MPPT algorithm, the time-domain waveform of the reference dc-link voltage $v_{\text{dc}}^*(t)$ has a fundamental period of $T_0 = 4T_{\text{MPPT}}$ (in the steady-state operation), as it is shown in Fig. 15. Thus, the reference dc-link voltage $v_{\text{dc}}^*(t)$ can be expressed as

$$v_{\text{dc}}^*(t) = \begin{cases} V_{\text{dc}}, & 0 \le t < T_{\text{MPPT}} \\ V_{\text{dc}} + v_{\text{step}}, & T_{\text{MPPT}} \le t < 2T_{\text{MPPT}} \\ V_{\text{dc}}, & 2T_{\text{MPPT}} \le t < 3T_{\text{MPPT}} \\ V_{\text{dc}} - v_{\text{step}}, & 3T_{\text{MPPT}} \le t < 4T_{\text{MPPT}} \end{cases} \quad (1)$$

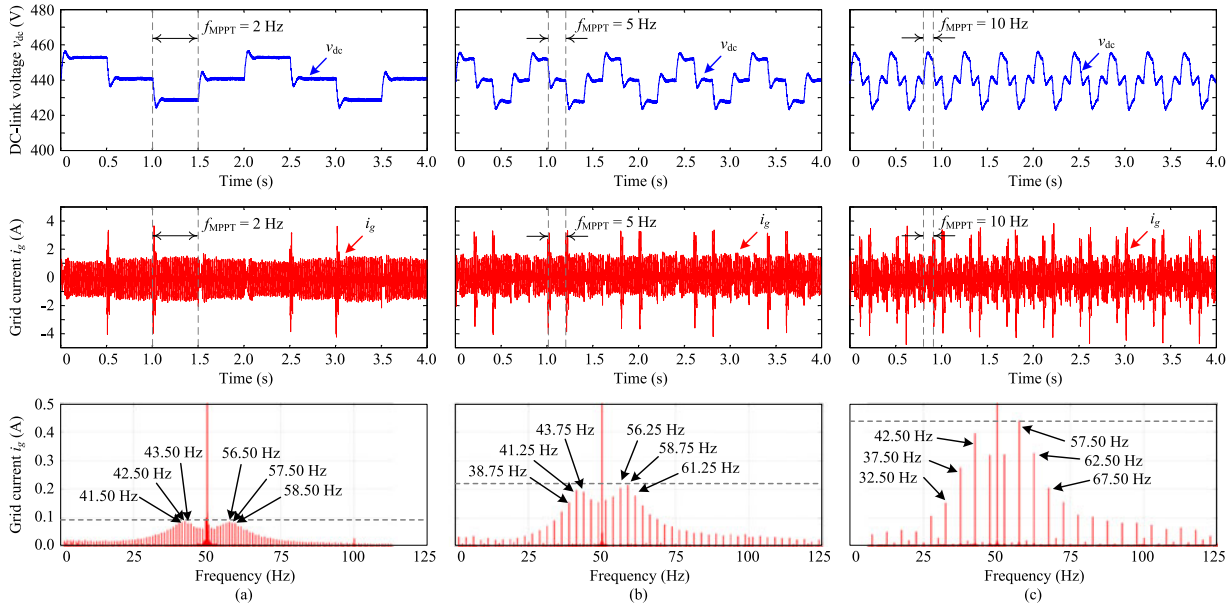

Fig. 13. Experimental results of the PV system operating at 10% of the rated power (i.e., 300 W) with the MPPT algorithm sampling rate of (a) $f_{\text{MPPT}} = 2$ Hz, (b) $f_{\text{MPPT}} = 5$ Hz, and (c) $f_{\text{MPPT}} = 10$ Hz, where v_{dc} is the dc-link voltage (PV voltage), and i_g is the grid current.

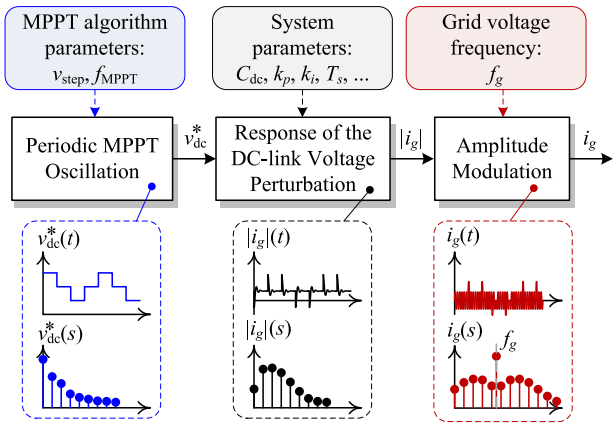

Fig. 14. Proposed modeling approach to identify interharmonics in the grid current due to the MPPT perturbation.

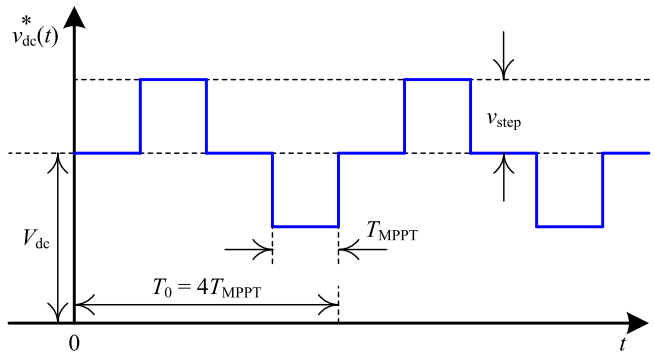

Fig. 15. Time-domain waveform of the reference dc-link voltage during the steady-state MPPT operation, where v_{step} is the perturbation step size and $T_{\text{MPPT}} = 1/f_{\text{MPPT}}$ is the MPPT sampling period.

where $T_{\text{MPPT}} = 1/f_{\text{MPPT}}$ is the MPPT sampling period and V_{dc} is the average dc-link voltage. It can be noticed that the time-domain expression of the reference dc-link voltage in (1) is a function of the perturbation step size v_{step} and the MPPT sampling rate f_{MPPT}, which is also observed in Section III. In this way, the influence of the MPPT algorithm parameters on the interharmonics in the grid current can be analyzed.

Applying the Fourier analysis to the time-domain function of the reference dc-link voltage in (1) gives

$$v^*_{\text{dc}}(t) = \frac{a_0}{2} + \sum_{n=1}^{\infty}\Big(a_n \cos(\omega_n t) + b_n \sin(\omega_n t)\Big)$$
$$= \frac{a_0}{2} + \sum_{n=1}^{\infty}\left(a_n \cos\left(\frac{2\pi n t}{T_0}\right) + b_n \sin\left(\frac{2\pi n t}{T_0}\right)\right) \quad (2)$$

with

$$a_0 = 2V_{\text{dc}},\ a_n = \frac{2v_{\text{step}}}{\pi n}\sin\left(\tfrac{\pi n}{2}\right),\ b_n = \frac{v_{\text{step}}}{\pi n}\cos(\pi n - 1)$$

in which n denotes the harmonic order with the fundamental period of $T_0 = 4T_{\text{MPPT}}$, a_0 is the Fourier coefficient of the dc component, and a_n and b_n are the Fourier coefficients of the nth order harmonic. In fact, the dc component a_0 can be neglected in a small-signal analysis (which is used for modeling the system response). According to (2), the reference dc-link voltage is decomposed into a set of periodic signals with the frequencies corresponding to integer times of the fundamental frequency $f_0 = 1/T_0$.

The Fourier analysis can also be represented with a single sinusoid, where the reference dc-link voltage at the nth order

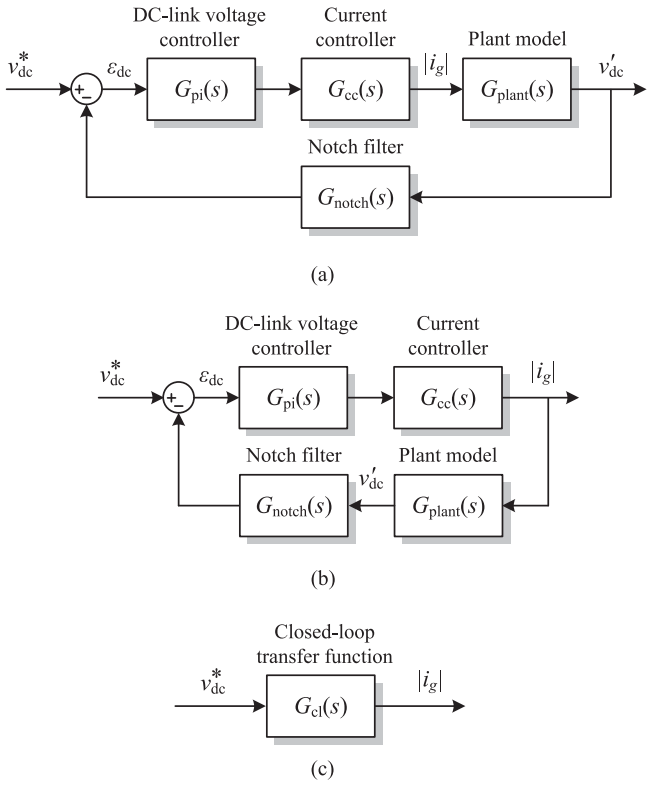

Fig. 16. Block diagrams of the dc-link voltage control loop: (a) transfer functions from the reference dc-link voltage $v_{\rm dc}^*$ to the measured dc-link voltage $v_{\rm dc}'$, (b) transfer functions from the reference dc-link voltage $v_{\rm dc}^*$ to the amplitude of the grid current $|i_g|$, and (c) the closed-loop transfer function.

harmonic $v_{{\rm dc}n}^*(t)$ can be expressed as

$$v_{{\rm dc}n}^*(t) = A_n \sin(\omega_n t + \phi_n) \tag{3}$$

$$v_{\rm dc}^*(t) = \sum_{n=1}^{\infty} v_{{\rm dc}n}^*(t) = \sum_{n=1}^{\infty} A_n \sin(\omega_n t + \phi_n)$$

with

$$A_n = \sqrt{a_n^2 + b_n^2},\ \phi_n = \tan^{-1}(a_n/b_n).$$

B. Response of the DC-Link Voltage Perturbation

Once the reference dc-link voltage $v_{\rm dc}^*(t)$ is decomposed into a summation of n frequency components, it can be used as an input to determine the controller response and also the output response of each frequency component. First, the transfer functions of different controllers in the dc-link voltage control loop are needed. The dc-link voltage control loop can be modeled as shown in Fig. 16(a) [40], [41], where $G_{\rm pi}(s)$ is the transfer function of the dc-link voltage controller (i.e., a PI controller), $G_{\rm cc}(s)$ is the transfer function of the current controller, $G_{\rm plant}(s)$ is the transfer function of the plant model (assuming a no-loss condition), and $G_{\rm notch}(s)$ is the transfer function of the notch filter employed in the feedback loop. Notably, this model is based on an assumption that the current control (inner loop) dynamics are much faster than the dc-link voltage control (outer loop) dynamics, and thereby they are decoupled from each other [41]. This is also practical in many applications. The details of each transfer function are given as

$$G_{\rm pi}(s) = k_p + \frac{k_i}{s}, \qquad G_{\rm cc}(s) = \frac{1}{1+3T_s s}$$

$$G_{\rm plant}(s) = \frac{V_g}{\sqrt{2}V_{\rm dc}C_{\rm dc}s}, \quad G_{\rm notch}(s) = \frac{s^2+\omega_h^2}{s^2+k_h s+\omega_h^2} \tag{4}$$

where k_p and k_i are the proportional and integral gain of the dc-link voltage controller, respectively, T_s is the digital controller sampling period, V_g is the root-mean-square (RMS) value of the grid voltage, $V_{\rm dc}$ is the average dc-link voltage (which is the condition where the linearization takes place), ω_h is the notch frequency (e.g., $\omega_h = 2\pi \times 100$ rad/s), and k_h represents the quality factor of the notch filter.

The dc-link voltage control loop can then be rearranged in order to determine the response of the grid current amplitude $|i_g|$ due to the dc-link voltage perturbation, as it is shown in Fig. 16(b). The block diagram can be further simplified in order to determine the closed-loop transfer function $G_{\rm cl}(s)$ between the reference dc-link voltage $v_{\rm dc}^*$ and the grid current amplitude $|i_g|$ as in Fig. 16(c), which is given as

$$G_{\rm cl}(s) = \frac{G_{\rm pi}(s)\cdot G_{\rm cc}(s)}{1 + G_{\rm notch}(s)\cdot G_{\rm plant}(s)\cdot G_{\rm pi}(s)\cdot G_{\rm cc}(s)}$$

$$= \frac{\left(k_p + \frac{k_i}{s}\right)\left(\frac{1}{1+3T_s s}\right)}{1 + \left(\frac{s^2+\omega_h^2}{s^2+k_h s+\omega_h^2}\right)\left(\frac{V_g}{\sqrt{2}V_{\rm dc}C_{\rm dc}s}\right)\left(k_p + \frac{k_i}{s}\right)\left(\frac{1}{1+3T_s s}\right)}.$$

During the steady state, a frequency response of the closed-loop transfer function can be represented as $G_{\rm cl}(j\omega)$. At each particular frequency ω_n, the frequency response of the closed-loop transfer function $G_{\rm cl}(j\omega_n)$ becomes $|G_{\rm cl}(j\omega_n)|\angle G_{\rm cl}(j\omega_n)$. Thus, the amplitude of the grid current at the nth order harmonic $|i_g|_n(t)$ can be determined as

$$|i_g|_n(t) = A_n|G_{\rm cl}(j\omega_n)|\sin(\omega_n t + \phi_n + \angle G_{\rm cl}(j\omega_n)). \tag{5}$$

Then, according to the superposition principle, the amplitude of the grid current $|i_g|(t)$ can be obtained by summing up all the frequency components as

$$|i_g|(t) = \sum_{n=1}^{\infty} |i_g|_n(t)$$

$$= \sum_{n=1}^{\infty} A_n|G_{\rm cl}(j\omega_n)|\sin(\omega_n t + \phi_n + \angle G_{\rm cl}(j\omega_n))$$

$$= \sum_{n=1}^{\infty} A_n' \sin(\omega_n t + \phi_n')$$

with

$$A_n' = A_n|G_{\rm cl}(j\omega_n)|,\ \phi_n' = \phi_n + \angle G_{\rm cl}(j\omega_n)$$

where it can be seen that the frequency response of the closed-loop transfer function has modified the amplitude (and also the phase angle) of the input signal. However, it has no contribution to the change in the interharmonic frequencies. This is observed in an example of the frequency spectrum of the reference

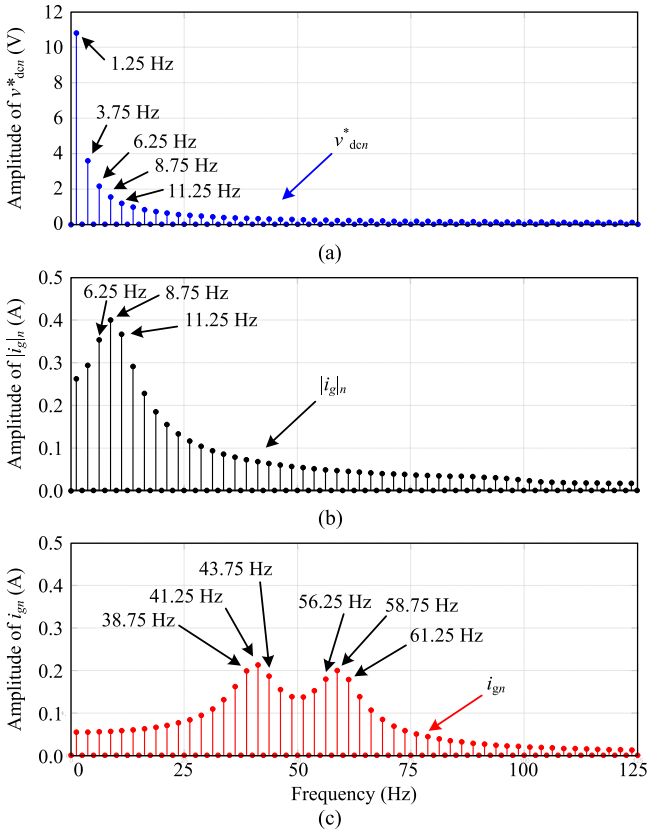

Fig. 17. An example of the frequency spectrum obtained from the proposed interharmonic model: (a) reference dc-link voltage v^*_{dcn}, (b) amplitude of the grid current $|i_g|_n$, and (c) grid current i_{gn}.

dc-link voltage and the amplitude of the grid current as shown in Fig. 17(a) and (b), respectively.

C. Amplitude Modulation

Following the control structure in Fig. 10, the grid current $i_g(t)$ is determined by multiplying the amplitude of the grid current $|i_g|(t)$ with the phase of the grid voltage $\sin(\theta_g)$, where $\theta_g = 2\pi f_g t$. Since the amplitude of the grid current contains a wideband spectrum as $|i_g|(t) = \sum_{n=1}^{\infty} |i_g|_n(t)$, the multiplication between the amplitude of the grid current $|i_g|(t)$ and the phase $\sin(\theta_g)$ will result in an amplitude modulation. This can be mathematically derived as

$$\begin{aligned} |i_g|_n(t)\sin(\theta_g) &= |i_g|_n(t)\sin(2\pi f_g t) \\ &= A_n^{'}\sin\left(\omega_n t + \phi_n^{'}\right)\sin(2\pi f_g t) \\ &= \frac{A_n^{'}}{2}\Big[\cos\left(2\pi t(f_g - f_n) + \phi_n^{'}\right) \\ &\quad - \cos\left(2\pi t(f_g + f_n) + \phi_n^{'}\right)\Big] \end{aligned} \tag{6}$$

which indicates that the nth order harmonic of the amplitude grid current $|i_g|_n$ will contribute to two frequency components: $f_g \pm f_n$. The amplitude of each resultant frequency component is equal to the half of the original signal amplitude, and the phase is shifted by $\pi/2$. For instance, the 8.75-Hz component

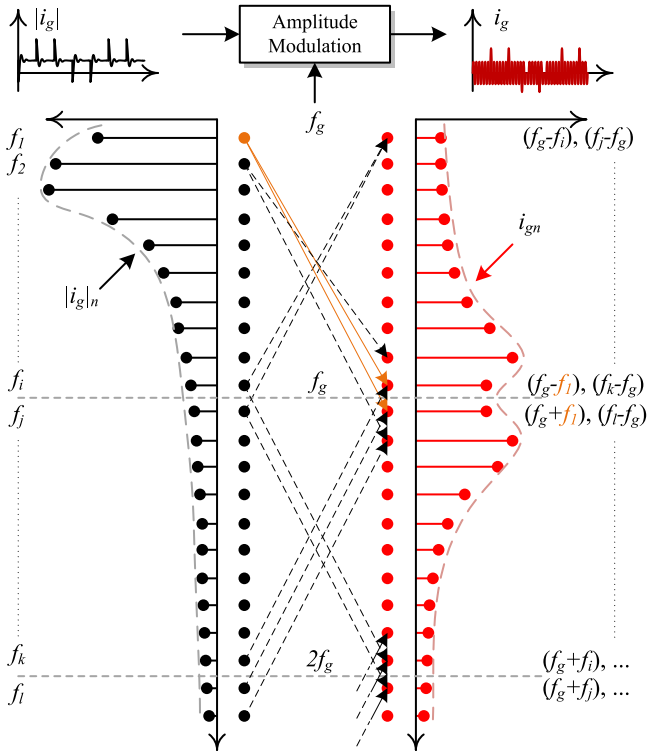

Fig. 18. Frequency mapping of the grid current i_g according to the amplitude modulation between the amplitude of the grid current $|i_g|$ and the phase of the grid voltage $\sin(\theta_g)$.

of the grid current amplitude $|i_g|$ in Fig. 17(b) will contribute to the components of 41.25 and 58.75 Hz appearing in the grid current i_g, as it is demonstrated in Fig. 17(c).

It should be pointed out that the frequency mapping between the input and the output signal is not a simple one-to-one mapping after the amplitude modulation, as illustrated in Fig. 18. Therefore, each interharmonic component of the grid current is the sum of two modulated signals which have equal frequency difference. By taking all frequency components into consideration, the grid current can be calculated as

$$\begin{aligned} i_g(t) = |i_g|(t)\sin(\theta_g) &= \sum_{n=1}^{\infty} |i_g|_n(t)\sin(2\pi f_g t) \\ &= \sum_{n=1}^{\infty} A_n^{'}\sin\left(\omega_n t + \phi_n^{'}\right)\sin(2\pi f_g t) \\ &= \sum_{n=1}^{\infty} \frac{A_n^{'}}{2}\Big[\cos\left(2\pi t(f_g - f_n) + \phi_n^{'}\right) \\ &\quad - \cos\left(2\pi t(f_g + f_n) + \phi_n^{'}\right)\Big]. \end{aligned} \tag{7}$$

D. Model Validation and Discussion

In order to validate the model and also the previous observations, the interharmonic model is applied to the PV system with different controller parameters: the MPPT perturbation step size v_{step} and the sampling rate of the MPPT algorithm f_{MPPT}. Then, the obtained results from the proposed model are compared with

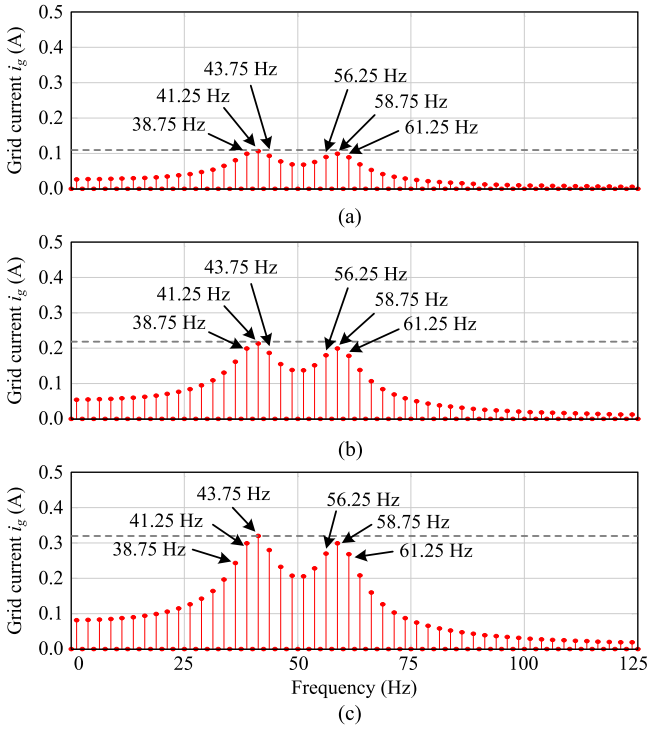

Fig. 19. Frequency spectrum of the grid current i_g (excluding the fundamental-frequency component f_g) obtained from the proposed interharmonic model with the MPPT perturbation step size of (a) $v_{\text{step}} = 6$ V, (b) $v_{\text{step}} = 12$ V, and (c) $v_{\text{step}} = 18$ V.

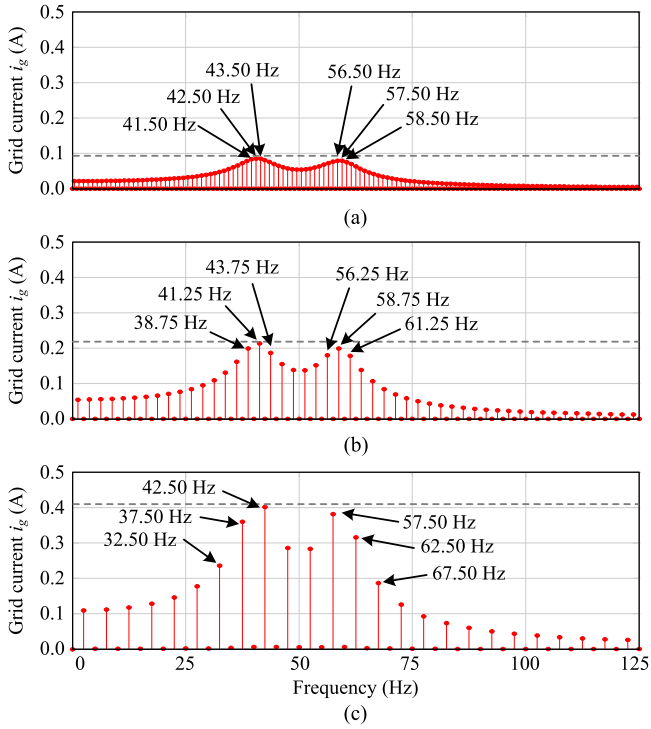

Fig. 20. Frequency spectrum of the grid current i_g (excluding the fundamental-frequency component f_g) obtained from the proposed interharmonic model with the MPPT sampling rate of (a) $f_{\text{MPPT}} = 2$ Hz, (b) $f_{\text{MPPT}} = 5$ Hz, and (c) $f_{\text{MPPT}} = 10$ Hz.

the experimental results under the same operating condition, as shown in Section III.

The influence of the perturbation step size on the interharmonic in the grid current is demonstrated in Fig. 19. In this case, three different perturbation step sizes of $v_{\text{step}} = 6$, 12, and 18 V are employed (same as the case in Fig. 12). It can be seen in Fig. 19 that the amplitude of the interharmonic increases as the amplitude of the perturbation step size increases, while the interharmonic frequency remains unchanged. The results obtained from the proposed model are in a close agreement with the experimental results in Fig. 12 both in terms of the interharmonic frequency and the amplitude of each individual component.

Furthermore, the operating condition with different MPPT sampling rates is also demonstrated in Fig. 20, where the MPPT sampling rates of $f_{\text{MPPT}} = 2$, 5, and 10 Hz (same as the case in Fig. 13) are applied to the proposed model. It can be observed in Fig. 20 that the distance between the two consecutive interharmonic frequencies increases as the MPPT sampling frequency increases. The interharmonic frequency also matches well with the observed experimental results in Fig. 13. In fact, the amplitudes of the interharmonic components from the proposed model shown in Fig. 20 are also in a close agreement with the experiments in Fig. 13.

From the above results, it can be seen that the interharmonics in the grid current can be predicted and analyzed with the proposed model, where the results agree well with the experiments. Therefore, the effectiveness of the proposed model is validated. Moreover, it can be used as a tool to design the controller parameters according to the specific interharmonic requirements, if they are required by standards. In addition, possible mitigation solutions have been discussed through simulations in [30]. However, more comprehensive study including the experimental validation is still required in this field.

It is worth mentioning that this paper only focuses on the interharmonic emission mechanism related to the MPPT operation, which is unique for the PV systems. In reality, there could be other sources of interharmonics. For instance, they can be either generated by the PV inverter itself or induced through the interaction between PV inverters and other power electronic units. This requires further investigation, where variations in the grid condition (e.g., stiff and nonstiff grid) should be one consideration. Moreover, only the P&O MPPT algorithm is considered in this study, where the power oscillation occurs during the steady-state operation. This behavior also applies to other hill-climbing-type MPPT algorithms such as the incremental conductance MPPT algorithm [42], where the above analysis can be applied with minor modifications. In order to further apply the analysis discussed in this paper to the other MPPT algorithms, it is necessary to model the steady-state behavior of the corresponding algorithm (e.g., if it causes power oscillation or not) in the frequency domain by analyzing the frequency spectrum of the dc-link voltage. Afterwards, the same approach as discussed in Fig. 14 can be followed.

V. Conclusion

In this paper, the interharmonics were observed experimentally in PV systems, and thus the mechanisms were ex-

plored. First, the observations from experiments showed that the perturbation from the MPPT algorithm is one of the main causes of interharmonics. A further exploration has demonstrated that the interharmonics appear in the grid current due to the amplitude modulation between the response of the dc-link voltage (i.e., amplitude of the grid current) and the phase of the grid voltage. The interharmonic characteristics were also investigated under different controller parameters. It turned out that the perturbation step size of the MPPT algorithm has a strong influence on the amplitudes of the interharmonic components. On the other hand, the MPPT sampling rate affects both the amplitude and the frequency of the interharmonics. Based on the experimental observations, a model of interharmonics was proposed in this paper. The interharmonic model was then used to identify the characteristics of interharmonics in PV systems under the same conditions of experiments. Comparisons with the experiments validated the effectiveness of the proposed model. Hence, this model can be used to predict and analyze interharmonics in PV systems. It can also be a guiding tool to design the controller.

REFERENCES

[1] A. R. Oliva and J. C. Balda, "A PV dispersed generator: A power quality analysis within the IEEE 519," *IEEE Trans. Power Del.*, vol. 18, no. 2, pp. 525–530, Apr. 2003.

[2] F. Katiraei, K. Mauch, and L. Dignard-Bailey, "Integration of photovoltaic power systems in high-penetration clusters for distribution networks and mini-grids," *Int. J. Distrib. Energy Resources*, vol. 3, no. 3, pp. 207–223, 2007.

[3] E. Fuchs and M. A. Masoum, *Power Quality in Power Systems and Electrical Machines*. New York, NY, USA: Academic, 2008.

[4] F. Katiraei and J. R. Aguero, "Solar PV integration challenges," *IEEE Power Energy Mag.*, vol. 9, no. 3, pp. 62–71, May 2011.

[5] F. Blaabjerg, Y. Yang, D. Yang, and X. Wang, "Distributed power-generation systems and protection," *Proc. IEEE*, vol. 105, no. 7, pp. 1311–1331, Jul. 2017.

[6] C. Li, "Unstable operation of photovoltaic inverter from field experiences," *IEEE Trans. Power Del.*, doi: 10.1109/TPWRD.2017.2656020, to be published.

[7] D. G. Infield, P. Onions, A. D. Simmons, and G. A. Smith, "Power quality from multiple grid-connected single-phase inverters," *IEEE Trans. Power Del.*, vol. 19, no. 4, pp. 1983–1989, Oct. 2004.

[8] J. H. R. Enslin and P. J. M. Heskes, "Harmonic interaction between a large number of distributed power inverters and the distribution network," *IEEE Trans. Power Electron.*, vol. 19, no. 6, pp. 1586–1593, Nov. 2004.

[9] D. Gallo *et al.*, "Case studies on large PV plants: Harmonic distortion, unbalance and their effects," in *Proc. IEEE Power Energy Soc. Gen. Meeting*, Jul. 2013, pp. 1–5.

[10] R. K. Varma, S. A. Rahman, T. Vanderheide, and M. D. N. Dang, "Harmonic impact of a 20-MW PV solar farm on a utility distribution network," *IEEE Power Energy Technol. Syst. J.*, vol. 3, no. 3, pp. 89–98, Sep. 2016.

[11] T. Messo, J. Jokipii, A. Aapro, and T. Suntio, "Time and frequency-domain evidence on power quality issues caused by grid-connected three-phase photovoltaic inverters," in *Proc. 16th Eur. Conf. Power Electron. Appl.*, Aug. 2014, pp. 1–9.

[12] Y. Yang, K. Zhou, and F. Blaabjerg, "Current harmonics from single-phase grid-connected inverters—Examination and suppression," *IEEE J. Emerg. Sel. Topics Power Electron.*, vol. 4, no. 1, pp. 221–233, Mar. 2016.

[13] S.-G. Jeong and M.-H. Park, "The analysis and compensation of dead-time effects in PWM inverters," *IEEE Trans. Ind. Electron.*, vol. 38, no. 2, pp. 108–114, Apr. 1991.

[14] Y. Du, D. D.-C. Lu, G. James, and D. J. Cornforth, "Modeling and analysis of current harmonic distortion from grid connected PV inverters under different operating conditions," *Sol. Energy*, vol. 94, pp. 182–194, Aug. 2013.

[15] Y. Du, D. D.-C. Lu, G. M. L. Chu, and W. Xiao, "Closed-form solution of time-varying model and its applications for output current harmonics in two-stage PV inverter," *IEEE Trans. Sustain. Energy*, vol. 6, no. 1, pp. 142–150, Jan. 2015.

[16] P. Koponen, H. Hansen, and M. Bollen, "Interharmonics and light flicker," in *Proc. 23rd Int. Conf. Elect. Distrib.*, Jun. 2015, Paper 1100.

[17] M. Aiello, A. Cataliotti, S. Favuzza, and G. Graditi, "Theoretical and experimental comparison of total harmonic distortion factors for the evaluation of harmonic and interharmonic pollution of grid-connected photovoltaic systems," *IEEE Trans. Power Del.*, vol. 21, no. 3, pp. 1390–1397, Jul. 2006.

[18] G. Chicco, J. Schlabbach, and F. Spertino, "Experimental assessment of the waveform distortion in grid-connected photovoltaic installations," *Sol. Energy*, vol. 83, no. 7, pp. 1026–1039, Jul. 2009.

[19] R. Langella, A. Testa, S. Z. Djokic, J. Meyer, and M. Klatt, "On the interharmonic emission of PV inverters under different operating conditions," in *Proc. 2016 17th Int. Conf. Harmonics Quality Power*, Oct. 2016, pp. 733–738.

[20] R. Langella, A. Testa, J. Meyer, F. Mller, R. Stiegler, and S. Z. Djokic, "Experimental-based evaluation of PV inverter harmonic and interharmonic distortion due to different operating conditions," *IEEE Trans. Instrum. Meas.*, vol. 65, no. 10, pp. 2221–2233, Oct. 2016.

[21] P. Pakonen, A. Hilden, T. Suntio, and P. Verho, "Grid-connected PV power plant induced power quality problems—Experimental evidence," in *Proc. 18th Eur. Conf. Power Electron. Appl.*, Sep. 2016, pp. 1–10.

[22] X. Xu *et al.*, "Analysis and modelling of power-dependent harmonic characteristics of modern PE devices in LV networks," *IEEE Trans. Power Del.*, vol. 32, no. 2, pp. 1014–1023, Apr. 2017.

[23] A. Testa *et al.*, "Interharmonics: Theory and modeling," *IEEE Trans. Power Del.*, vol. 22, no. 4, pp. 2335–2348, Oct. 2007.

[24] M. Karimi-Ghartemani and and M. R. Iravani, "Measurement of harmonics/inter-harmonics of time-varying frequencies," *IEEE Trans. Power Del.*, vol. 20, no. 1, pp. 23–31, Jan. 2005.

[25] M. R. Rifai, T. H. Ortmeyer, and W. J. McQuillan, "Evaluation of current interharmonics from AC drives," *IEEE Trans. Power Del.*, vol. 15, no. 3, pp. 1094–1098, Jul. 2000.

[26] F. D. Rosa, R. Langella, A. Sollazzo, and A. Testa, "On the interharmonic components generated by adjustable speed drives," *IEEE Trans. Power Del.*, vol. 20, no. 4, pp. 2535–2543, Oct. 2005.

[27] H. Soltani, F. Blaabjerg, F. Zare, and P. C. Loh, "Effects of passive components on the input current interharmonics of adjustable-speed drives," *IEEE J. Emerg. Sel. Topics Power Electron.*, vol. 4, no. 1, pp. 152–161, Mar. 2016.

[28] L. F. Beites, J. G. Mayordomo, A. Hernandez, and R. Asensi, "Harmonics, interharmonics and unbalances of arc furnaces: A new frequency domain approach," *IEEE Trans. Power Del.*, vol. 16, no. 4, pp. 661–668, Oct. 2001.

[29] C. Vilar, J. Usaola, and H. Amaris, "A frequency domain approach to wind turbines for flicker analysis," *IEEE Trans. Energy Convers.*, vol. 18, no. 2, pp. 335–341, Jun. 2003.

[30] A. Sangwongwanich, Y. Yang, D. Sera, and F. Blaabjerg, "Interharmonics from grid-connected PV systems: Mechanism and mitigation," in *Proc. 2017 IEEE 3rd Int. Future Energy Electron. Conf. ECCE Asia*, Jun. 2017, pp. 722–727.

[31] Chroma, "Programmable DC power supply (solar array simulation) model 62000H-S series." [Online]. Available: http://www.chromausa.com/pdf/62000H-S-E.pdf

[32] F. Blaabjerg, R. Teodorescu, M. Liserre, and A. V. Timbus, "Overview of control and grid synchronization for distributed power generation systems," *IEEE Trans. Ind. Electron.*, vol. 53, no. 5, pp. 1398–1409, Oct. 2006.

[33] M. Ciobotaru, "Reliable grid condition detection and control of single-phase distributed power generation systems," Ph.D. dissertation, Dept. Energy Technol., Aalborg Univ., Aalborg, Denmark, 2009.

[34] Y. Yang, Z. Xin, K. Zhou, and F. Blaabjerg, "Unified digital periodic signal filters for power converter systems," in *Proc. 2017 IEEE 3rd Int. Future Energy Electron. Conf. ECCE Asia*, Jun. 2017, pp. 286–291.

[35] T. Esram and P. L. Chapman, "Comparison of photovoltaic array maximum power point tracking techniques," *IEEE Trans. Energy Convers.*, vol. 22, no. 2, pp. 439–449, Jun. 2007.

[36] N. Femia, G. Petrone, G. Spagnuolo, and M. Vitelli, "Optimization of perturb and observe maximum power point tracking method," *IEEE Trans. Power Electron.*, vol. 20, no. 4, pp. 963–973, Jul. 2005.

[37] N. Femia, G. Petrone, G. Spagnuolo, and M. Vitelli, "Optimizing sampling rate of P&O MPPT technique," in *Proc. Power Electron. Spec. Conf.*, Jun. 2004, vol. 3, pp. 1945–1949.

[38] M. Rosu-Hamzescu and and S. Oprea, "Practical guide to implementing solar panel MPPT algorithms," Microchip Technol., Inc., Chandler, AZ, USA, 2013.

[39] J. Kivimaki, S. Kolesnik, M. Sitbon, T. Suntio, and A. Kuperman, "Revisited perturbation frequency design guideline for direct fixed-step maximum power point tracking algorithms," *IEEE Trans. Ind. Electron.*, vol. 64, no. 6, pp. 4601–4609, Jun. 2017.

[40] V. Blasko and V. Kaura, "A new mathematical model and control of a three-phase AC-DC voltage source converter," *IEEE Trans. Power Electron.*, vol. 12, no. 1, pp. 116–123, Jan. 1997.
[41] R. Teodorescu, M. Liserre, and P. Rodriguez, *Grid Converters for Photovoltaic and Wind Power Systems*. New York, NY, USA: IEEE-Wiley, 2011.
[42] D. Sera, L. Mathe, T. Kerekes, S. V. Spataru, and R. Teodorescu, "On the perturb-and-observe and incremental conductance MPPT methods for PV systems," *IEEE J. Photovolt.*, vol. 3, no. 3, pp. 1070–1078, Jul. 2013.

Ariya Sangwongwanich (S'15) received the B.Eng. degree in electrical engineering in 2013 from Chulalongkorn University, Bangkok, Thailand, and the M.Sc. degree in energy engineering in 2015 from Aalborg University, Aalborg, Denmark, where he is currently working toward the Ph.D. degree.

His research interests include control of grid-connected converter, photovoltaic systems, reliability in power electronics, and high-power multilevel converters.

Yongheng Yang (S'12–M'15–SM'17) received the B.Eng. degree in electrical engineering and automation from Northwestern Polytechnical University, Shaanxi, China, in 2009, and the Ph.D. degree in electrical engineering from Aalborg University, Aalborg, Denmark, in 2014.

He was a Postgraduate Student with Southeast University, Jiangsu, China, from 2009 to 2011. In 2013, he was a Visiting Scholar with Texas A&M University, College Station, TX, USA. Since 2014, he has been with the Department of Energy Technology, Aalborg University, where he is currently an Associate Professor. His research includes grid integration of renewable energies, power electronic converter design, analysis and control, and reliability in power electronics.

Dr. Yang served as a Guest Associate Editor for the IEEE JOURNAL OF EMERGING AND SELECTED TOPICS IN POWER ELECTRONICS and a Guest Editor for *Applied Sciences*. He is an Associate Editor for the *CPSS Transactions on Power Electronics and Applications*.

Dezso Sera (S'05–M'08–SM'15) received the B.Sc. and M.Sc. degrees in electrical engineering from the Technical University of Cluj, Cluj-Napoca, Romania, in 2001 and 2002, respectively, and the M.Sc. degree in power electronics and the Ph.D. degree in PV systems, both from the Department of Energy Technology, Aalborg University, Aalborg, Denmark, in 2005 and 2008, respectively.

Since 2009, he has been the Program Leader of the Photovoltaic Systems Research Programme (www.pv-systems.et.aau.dk) with the Department of Energy Technology, Aalborg University, where he is also currently an Associate Professor with the same department. His research interests include modeling, characterization, diagnostics and maximum power point tracking of PV arrays, as well as power electronics and grid integration for PV systems.

Hamid Soltani (S'14–M'16) received the B.Sc. and M.Sc. degrees in electrical engineering from the University of Mazandaran (Noushirvani), Babol, Iran, in 2005 and 2008, respectively, and the Ph.D. degree in power electronics from Aalborg University, Aalborg, Denmark, in 2016.

From 2009 to 2013, he was with the Department of Electrical and Computer Engineering, Golestan University, Gorgan, Iran, as a Lecturer. He was also a Postdoctoral Researcher with the Department of Energy Technology, Aalborg University, from May 2016 to June 2017. He is currently with the Department of Converter Control, Vestas Wind Systems A/S, Aarhus, Denmark. His current research interests include wind energies, power quality, and power electronics topologies and control.

Frede Blaabjerg (S'86–M'88–SM'97–F'03) received the Ph.D. degree in electrical engineering from Aalborg University, Aalborg, Denmark, in 1995.

He was with ABB-Scandia, Randers, Denmark, from 1987 to 1988. He became an Assistant Professor in 1992, an Associate Professor in 1996, and a Full Professor of power electronics and drives in 1998. His current research interests include power electronics and its applications such as in wind turbines, PV systems, reliability, harmonics, and adjustable speed drives.

Dr. Blaabjerg received 18 IEEE Prize Paper Awards, the IEEE PELS Distinguished Service Award in 2009, the EPE-PEMC Council Award in 2010, the IEEE William E. Newell Power Electronics Award 2014, and the Villum Kann Rasmussen Research Award 2014. He was an Editor-in-Chief for the IEEE TRANSACTIONS ON POWER ELECTRONICS from 2006 to 2012. He was nominated in 2014, 2015, 2016, and 2017 by Thomson Reuters to be between the most 250 cited researchers in engineering in the world.